Finite element analysis of the mechanical properties of sheet- and skeleton-gyroid Ti6Al4V structures produced by laser powder bed fusion

Zhichao Luo[a], Qian Tang[a,*], Qixiang Feng[b], Shuai Ma[c], Jun Song[a], Rossitza Setchi[d], Fuyu Guo[a], Yuanhang Zhang[a]

a. State Key Laboratory of Mechanical Transmissions, Chongqing University, Chongqing 400044, China

b. School of Smart Health, Chongqing College of Electronic Engineering. Chongqing 401331, China

c. College of Mechanical Engineering, Chongqing University of Technology, Chongqing, 400054, China

d. Cardiff School of Engineering, Cardiff University, Cardiff, CF24 3AA, United Kingdom

* Corresponding author: Qian Tang

Address: No. 174, Shazheng Street, Shapingba District, Chongqing 400044, China.

E-mail address: tqcqu@cqu.edu.cn

Abstract

Additive manufacturing, and laser powder bed fusion (L-PBF) in particular, can produce complex geometric components with high resolution, and is very suitable for manufacturing lightweight triple periodic minimal surface (TPMS) structures to achieve lightweight. With regard to the two forms of the same structure, most of the previous studies focused on sheet-TPMS, but lacked the understanding of the difference between skeleton-TPMS and sheet-TPMS structures. In order to explore the characteristics of these two structures and provide theoretical support for the development of lightweight structure design, this paper compares the manufacturing performance and defect distribution of skeleton-gyroid (G_{SK}) and sheet-gyroid structures (G_{SH}). It employs high-precision finite element analysis (FEA) prediction and experimental verification to compare comprehensively the mechanical properties, failure behavior and energy absorption characteristics of the two structures. The results show that, compared to G_{SK}, the larger specific surface area of G_{SH} leads to more unmelted powder and draping adhesion, without affecting its higher stiffness and strength. Moreover, the more stable failure mode of GSH leads to more gentle stress platform stage and superior energy absorption performance. The results predicted by

simulation are highly consistent with the experimental results. This improved understanding allows better prediction of the mechanical properties of the specimens using the Gibson-Ashby theory, which can reduce the experimental cost and time, and improve the resource consumption of TPMS structural performance research. This study can open new possibilities for the design and application of TPMS structures.

Keywords Laser powder bed fusion, Triply periodic minimal surface, Lightweight, Simulation, Mechanical properties

1 Introduction

Laser powder bed fusion (L-PBF) is currently one of the most effective powder bed-based additive manufacturing technologies, which uses a laser beam to selectively melt metal powders according to a three-dimensional computer-aided design (CAD) model. Due to its ability to free-form fine interconnected structures, L-PBF is considered a viable solution for fabricating porous metal structures. Consequently, the triple periodic minimal surface (TPMS) fabricated with L-PBF[1,2] has been widely fabricated as a typical porous structure[3] and widely used in the development of novel components such as biomedical implants[4-6], heat exchangers[7], aerospace structures[8], and impact engineering[9-11].

TPMS structure is a kind of periodic structure composed of cells. The mechanical properties of TPMS structures are affected by numerous design parameters, including the volume fraction (or relative density)[12], pore size[13,14], unit size[15,16], and unit topology[17,18], with the volume fraction being the most important factor[19]. Commonly seen L-PBF-produced TPMS structures are divided into two categories: skeleton-TPMS and sheet-TPMS[20-22]. Skeleton-TPMS is created by solidifying one of the volumes that the TPMS topology has partitioned, with the constant of the level approximation equation controlling the volume fraction. Sheet-TPMS involves giving the surface specific thickness that regulates the volume fraction while keeping the surface as a whole continuous and fixed[23].

Previous studies[24-26] use experiments combined with simulations to study sheet structures or skeletal structures individually. For example, the study conducted by Al-Ketan et al.[27] found that the sheet-based cellular structures possess excellent load-

bearing and energy absorption properties compared with traditional metallic foams. Fan et al.[28] used the method of functional graded modeling to design and study the manufacturability, mechanical properties and energy absorption capacity of three kinds of sheet structures, and compared them by compression test. The results show that the constant thickness sheet structures have better stiffness, strength and energy absorption capacity, while the graded thickness sheet structures have higher elastic modulus and cumulative energy absorption value. Sun et al.[29] revised the Gibson-Ashby prediction model based on the experimental results of three sheet structures, and analyzed the deformation mechanism of the structure using the finite element method. On this basis, the mechanical properties, energy absorption and relative density maps of the sheet structures were obtained. The result shows that the energy absorption capacity of the sheet structures increases with the increase of the actual relative density. Wen et al.[30] used numerical simulations, metamodels and NSGA-II algorithm to carry out multi-objective optimization design for four TPMS sheet structures. The results show that compared with other natural and engineering energy adsorbed structures, TPMS sheet structures, especially FRD-sheet structures, possess higher specific energy absorption and specific strength and have outstanding potential in future engineering applications. Yin et al.[31] used SF surface splicing method to splice three novel types of composite TPMS-based structure and studied the crashworthiness of structures with different thickness ratios under impact loading by finite element method. The results show that compared with traditional structures, TPMS-based composite structure has higher energy absorption efficiency, better energy absorption and lower peak crushing force, , which makes it have a good application prospect in aerospace and military industry.

There are relatively fewer studies on skeletal structures and comparisons of skeleton and sheet structures. Yang et al.[32] predicted the elastic modulus, compressive yield strength and stress/strain distribution of skeleton-gyroid structure by finite element method, and analyzed its failure mechanism. Alkentan et al.[33] and Abou-Ali et al.[34] compared the mechanical properties of skeleton-TPMS and sheet-TPMS structures with different volume fractions and found that the sheet-TPMS behaved stretching-dominated to present better load-bearing capacity than the skeletal-

TPMS.

Although the above studies investigated the TPMS mechanical properties, most of the research focused on the analysis of a single type of structure, resulting in the lack of in-depth understanding of skeleton- and sheet-TPMS structures. In addition, due to the complex geometry and difficult forming of TPMS structures, specimen tests are usually conducted to evaluate the mechanical behavior of these structures. However, the FEA method to predict the quasi-static behavior of TPMS structures is rarely employed to its full potential, resulting in low accuracy in simulating the mechanical properties and failure behavior of the structures.

In order to meet this challenge and provide more design options and potential applications of TPMS structures, this study designed and fabricated skeleton- and sheet-gyroid structures with three volume fractions, and compared their morphological differences and defect distribution. By combining high-precision simulation prediction (Johnson-Cook damage model) with experimental verification, it studied in detail the influence mechanism of mechanical properties, failure behavior and energy absorption characteristics of the two structures are investigated. This new understanding is of great significance, as it allows reduction of the number of experiments and resource consumption when exploring different lightweight design alternatives.

2 Materials and methods

In this section, the design methods, fabrication, and deformation study under compressive loading based on the gyroid structures are described. Then, the FEA models are created and the mechanical properties and energy absorption characteristics are presented.

2.1 Gyroid Lattice Structure Design

All models of the gyroid lattice structures were constructed using Rhino, and the post-processing of the corresponding STL files was performed in Materialise Magics. The gyroid models were fabricated using L-PBF.

The implicit equation of the gyroid surface is expressed as

$$\varphi_G(x,y,z) = \cos(k_x x)\cdot\sin(k_y y) + \cos(k_y y)\cdot\sin(k_z z) + \cos(k_z z)\cdot\sin(k_x x) - c = 0 \quad (1)$$

where $k_i = 2\pi n_i / L_i$ $(i = x, y, z)$, k_i controls the unit size in x, y, and z directions, L_i is the unit length along x, y, and z axis, and n_i is the number of lattice units in x, y, and z axis in each unit.

For the G_{SK} and G_{SH} structures, the solid-void boundaries are defined by gyroid equations, and c is an offset parameter used to control the position of the solid-void boundary and the volume fraction of the lattice structures. Fig.1(a) shows the modelling process of G_{SK} and G_{SH} structures obtained by unidirectional and bilateral offset of isosurface respectively. It was found that there is a linear relationship between parameter c and the relative volume fraction V_f. For gyroid structures, these linear relationships are shown in Fig.1(b).

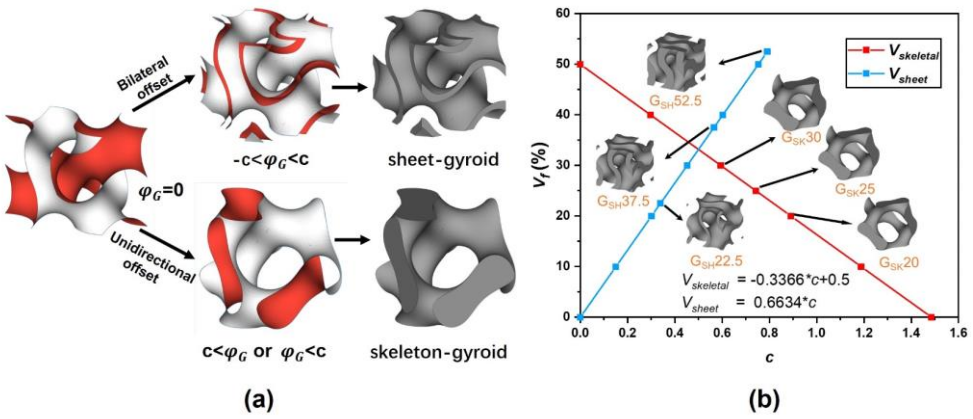

Fig. 1 (a) Modelling process of skeleton- and sheet-gyroid structures and (b) relationship between the volume fraction V_f and offset parameter c for gyroid.

Using different c values, skeletal structures with volume fractions of 20%, 25%, and 30% and sheet structures with volume fractions of 22.5%, 37.5%, and 52.5% were designed. Each structure consists of gyroid cell arrays of 3 × 3 × 3 mm^3.

For simplicity, the lattice structures were named using the pattern of $G_{()}()$. For example, a skeleton-gyroid and sheet-gyroid lattice structure specimens with 30% relative volume fraction were named $G_{SK}30$ and $G_{SH}30$, respectively. The six gyroid structures with dimensions 18 × 18 × 18 mm^3 and 6 × 6 × 6 unit cells.

2.2 Materials and Fabrication by L-PBF

As shown in Fig. 2, the gyroid specimens were fabricated using an L-PBF machine (SLM Solutions, Germany), with a laser power of 275 W, a scan strategy that rotated 57° between consecutive layers and other processing parameters given in Table 1. These specimens were finally removed from the base plate by wire electrical discharge machining. To remove the remaining powder from the surfaces of the samples, all the samples were cleaned by an ultrasonic cleaner immersed in isopropanol for 5 min. Each structure has three duplications without any other post-treatment or heat treatment after washing.

Table 1 Main parameters of the L-PBF-manufactured process

Parameter	Value
Laser power	275 W
Laser scanning speed	1100 mm/s
Laser scanning interval	110 μm
Laser spot diameter	80 μm
Powder deposition thickness	30 μm
Angle of adjacent layers	57°

An electronic analytical balance with accuracy 0.001g was used to measure the fabrication weight (23 °C) and wet weight (20 °C) of the fabricated specimens. The wet weight was measured in 0.79 g/ml alcohol. A digital calliper with an accuracy of 0.01 mm was used to measure the *x*, *y*, and *z* axis of the specimens, and the dimensions and variance were measured and counted. The actual volume fraction ($V_{f\ \text{specimen}}$) was calculated from the three-directional dimensions (L_x, L_y and L_z), average density (ρ), and measured dry weight (W) of the specimens, as shown in Equation (2):

$$V_{f\ \text{specimen}} = \frac{\mathrm{W}}{\rho \mathrm{L_x L_y L_z}} \tag{2}$$

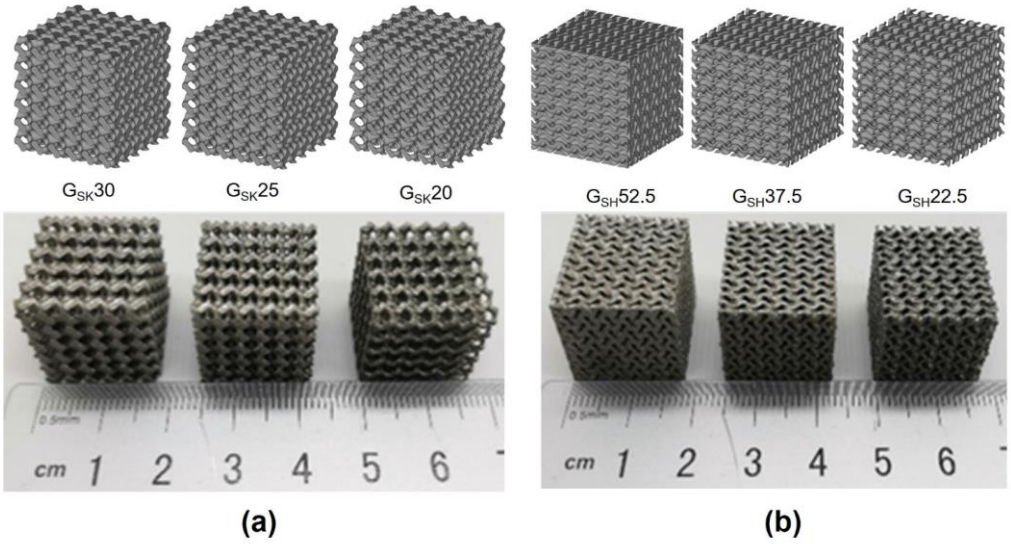

Fig. 2 Gyroid lattice structures: (a) G_{SK} structures and (b) G_{SH} structures

The average size of the Ti6Al4V powder was 37.33 μm as determined by a Mastersizer (S3500, Microtrac, USA). Block specimens manufactured alongside the lattices were used to determine the density of the Ti6Al4V material. A comparison of specimen masses and volumes yielded a density of 4.43 g/cm^3, which agrees well with the material provider's specifications. The chemical composition of the powder is shown in Table 2.

Table 2 Chemical constituents of Ti6Al4V powder

Ti6Al4V	Ti	Al	V	O	Fe
Wt.%	Allowance	6.78	4.32	0.16	0.07

2.3 Finite Element Analysis

Abaqus/Explicit 2021 software was used to predict the elastic modulus, yield strength, and peak stress of the specimens. As shown in Fig. 3, the mechanical properties were estimated by creating a compression model. The structural models were placed between two parallel plates, which were regarded as rigid materials. The bottom plate remained stationary while the top plate moved downward at a constant displacement of -9 mm, along the reverse direction along the z axis to compress the specimen by 50%, as shown in Fig. 3(a). The structural models were meshed with tetrahedral elements (C3D4), as shown in Fig. 3(b). The rigid plates were meshed with four-node linear quadrilateral elements (R3D4). A friction coefficient of 0.2 was set

between the rigid plates and the models to simulate the boundary conditions during the compression process.

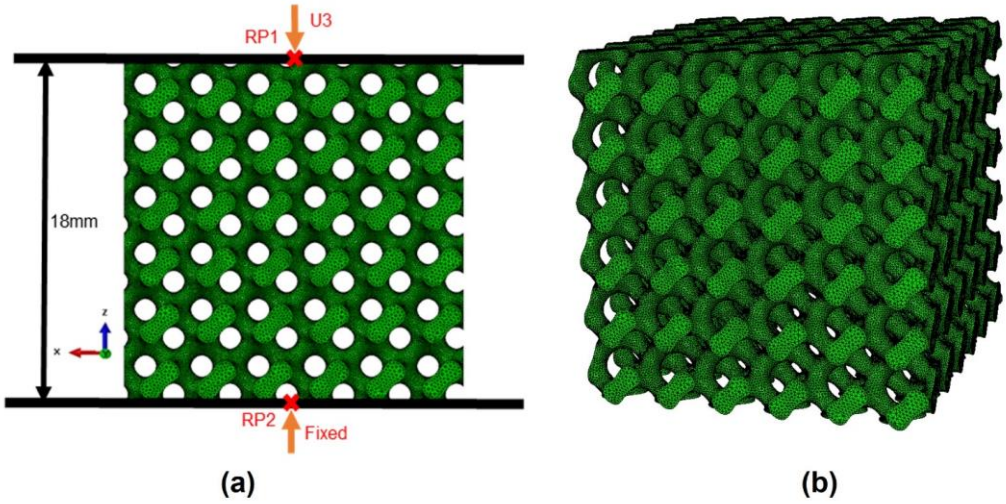

Fig. 3 FEA models of C3D4 meshes: (a) boundary conditions and (b) gyroid structural model.

2.3.1 Material model

The bulk material is Ti6Al4V with a density of 4.43 g/cm3, Young's modulus of 108,090 MPa, and Poisson's ratio of 0.3. As shown in Table 3, the input true plastic stress and strain parameters were based on the work of Jin et al.[35]. To simulate the damage of materials during compression, the Johnson-Cook damage model was specified in the material properties. The fracture strain ε_f is given by the following formula:

$$\varepsilon_f = (D_1 + D_2 \cdot exp(D_3\sigma^*)) \cdot (1 + D_4 ln(\dot{\varepsilon}^*_{eq})) \cdot (1 - D_5 T^*) \quad (3)$$

Where the D1, D2, D3, D4 and D5 are the material damage parameters obtained by the experiment. In this paper, the constant D4 and D5 are neglected due to the quasi-static compression process at room temperature. σ^* is the stress triaxiality, which is the ratio of hydrostatic pressure to equivalent stress. As shown in Table 4, the damage parameters of Johnson-Cook models for L-PBF Ti6Al4V refer to the data of Wang et al.[36].

Table 3 True plastic stress and strain of Ti6Al4V

Yield stress(MPa)	1189	1229	1253	1268	1282	1289	1294	1296
Plastic strain	0	0.002	0.004	0.006	0.009	0.012	0.016	0.02

Table 4 The property parameters set in the Johnson-Cook models for L-PBF Ti6Al4V

D_1	D_2	D_3	D_4	D_5
0.005	0.43	-0.48	0	0

2.3.2 Mesh sensitivity tests

Convergence is evaluated by the mesh sensitivity test to determine the effect of mesh size on the simulation results. A gyroid structure with a volume fraction of 20% was selected and tested in the mesh size range of 0.15 ~ 0.35 mm.

The curves in Fig.4 show that the elastic modulus and the yield strength decrease with the reduction of the element size. For mesh sizes less than 0.25 mm, the elastic modulus and yield strength tend to be constant. Larger meshes lead to unreliable results, while smaller meshes increase the calculation time. Therefore, the element size of 0.2 mm is considered the optimal mesh size for the convergence of the calculation process.

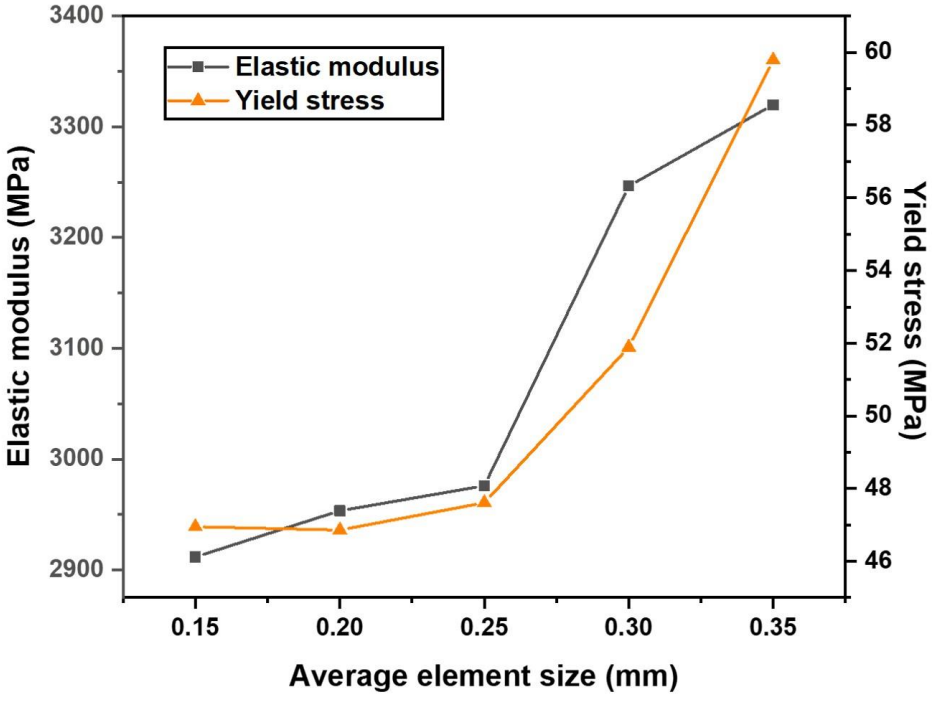

Fig. 4 Mesh sensitivity evaluation for the different element size

2.4 Mechanical and Energy Absorption Characterization

Compression tests were performed on the gyroid specimens in order to obtain the stress-strain curve of the gyroid structures and to investigate their damage mode. The compression testing equipment used here is a 300 KN SUNS WAW -600 universal testing machine. The loading force is applied to the top of the specimen through the upper crosshead, and the specimen is compressed at a speed of 2 mm/min. The stress and strain were calculated according to the following equations:

$$\sigma = \frac{F}{A} \tag{4}$$

$$\varepsilon = \frac{\Delta h}{h} \tag{5}$$

where σ is the stress (MPa), ε is the strain (%), F is the reaction force of the crosshead (N), A is the cross-sectional area of the specimen perpendicular to the z axis (mm^2), Δh is the displacement of the upper crosshead (mm), and h is the height of the specimen (mm).

The strain was calculated by dividing the displacement by the specimen height of 18 mm, and the stress was calculated by the load and the apparent cross-sectional area of 18 × 18 mm^2. Elastic modulus (E) was considered the slope of linear fits of the stress-strain curve at the elastic stage. The yield strength is based on the stress value that produces 0.2% residual deformation. Stress at the first peak of the experimental data was regarded as peak stress.

The mechanical performance prediction and structure comparison refer to the Gibson–Ashby theory[37]. The Gibson–Ashby formula is as follows:

$$\frac{E_S}{E_0} = C_E(\frac{\rho_S}{\rho_0})^{m_E} \tag{6}$$

$$\frac{\sigma_S}{\sigma_0} = C_\sigma(\frac{\rho_S}{\rho_0})^{m_\sigma} \tag{7}$$

where E_S, ρ_S, and σ_S are the elastic modulus, density, and yield strength of the gyroid structures, E_0, ρ_0, and σ_0 are the elastic modulus, density, and yield strength of the Ti6Al4V solid specimens, and C_E, C_σ, m_E, and m_σ are parameter values related to the material and the shape of the assembly. C_E and m_E are the modulus constants, C_σ

and m_σ are the strength constants. m_{E} and m_σ are related to the stress forms of the structure.

Energy absorption and energy absorption efficiency are defined as follows:

$$W = \int_0^\varepsilon \sigma(\varepsilon) d\varepsilon \tag{8}$$

$$W^e = \frac{\int_0^\varepsilon \sigma(\varepsilon) d\varepsilon}{\sigma(\varepsilon)} \tag{9}$$

where W is the energy absorption per unit volume, W^e is the energy absorption efficiency, ε is the strain, and $\sigma(\varepsilon)$ is the stress under the corresponding strain.

3 Results and Discussion

3.1 Morphology Characteristics

The densities of the specimens were measured using the Archimedes drainage method, as shown in Fig. 5(a). The measured density values of the specimens ranged from 4.417–4.424 g/mm^3, and the measurements showed that all density values of the specimens were above 99.95%, indicating that the difference between the bulk part and the gyroid part was very small and could be considered the same. Fig. 5(b) shows the lengths of the as-built specimens in three directions. Along the *x*-axis and *y*-axis, the error for all specimens was only 157–222 μm compared to the design value of 18 mm, indicating that the fabrication error was controlled in an acceptable range.. Along the *z* axis, all specimens were shorter than the design due to operational deviations during wire cutting.

The deviations between the designed and measured volume fractions ranged from 1.51% to 2.56%(G_{SK}) and 8.38% to 8.55%(G_{SH}), as shown in Table 5. The G_{SH} structures have larger specific surface area, resulting in more unmelted powders and overhanging adhesions, and therefore the variation in their volume fraction is larger.

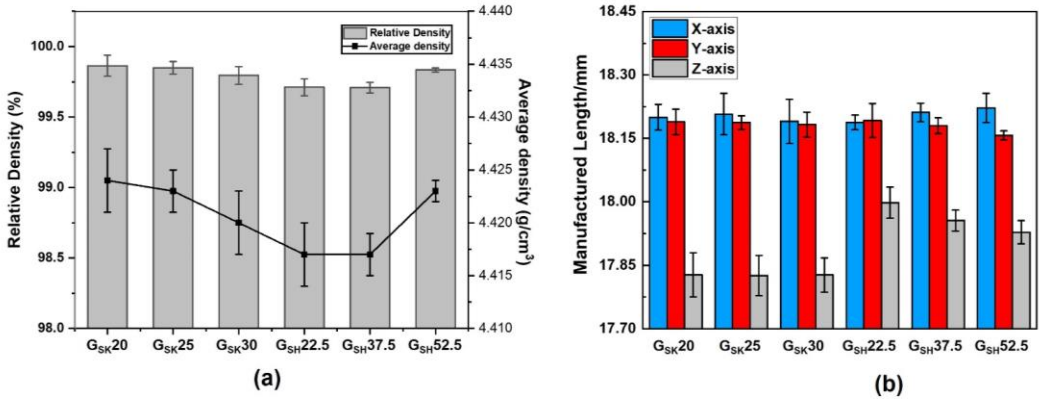

Fig. 5 (a) Average density and relative density of the as-built specimens and (b) manufactured length of the as-built specimens

Table 5 Manufactured volume fraction deviations of as-built specimens

Type	Volume fraction (%)		
	Average	Designed	Error
$G_{SK}20$	21.51±0.02	20	1.51
$G_{SK}25$	27.36±0.01	25	2.36
$G_{SK}30$	32.56±0.02	30	2.56
$G_{SH}22.5$	30.91±0.02	22.5	8.41
$G_{SH}37.5$	46.05±0.02	37.5	8.55
$G_{SH}52.5$	60.88±0.02	52.5	8.38

The morphological characteristics of the gyroid specimens were examined using an optical microscope (OM) to explore the factors affecting the volume fraction and specimen length. As shown in Fig. 6, unmelted powders adhere to the inner lattice surface, and overhanging structures are formed near the horizontal zones of the structures. This is due to the fact that the horizontal zones lack support, resulting in gravity-induced movement of the melted titanium alloy liquid, which eventually forms overhanging structures and increases the mass of the specimen[38-40]. Although the surface of the structures was rough, all units were intact and continuous, in addition to a stable rod diameter and wall thickness, showing that the structures were effectively self-supporting.

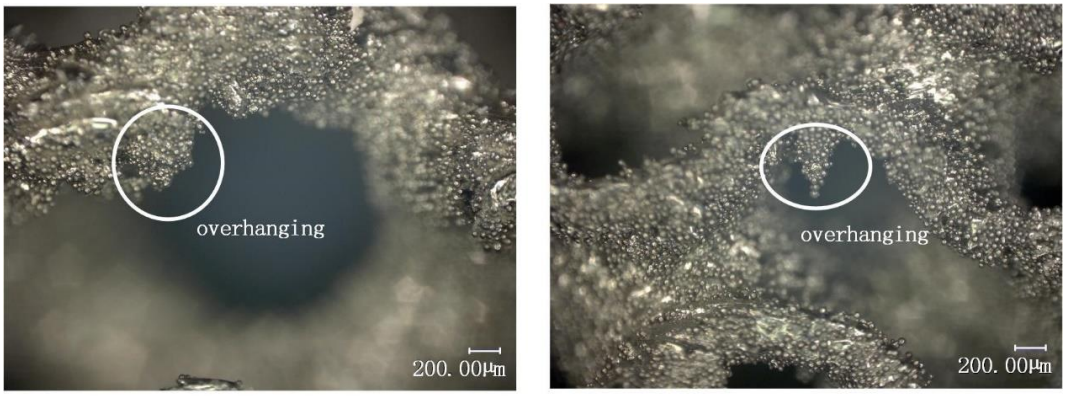

(a) (b)

Fig. 6 Amplification of gyroid structures: (a) G_{SK} structure and (b) G_{SH} structure

3.2 Elastoplastic Properties

The elastoplastic properties of the G_{SK} and G_{SH} structures were determined with three sets of repeated tests for each. Fig. 7(a-f) show the stress–strain curves of the compression tests. Good repeatability was found for all stress-strain curves for each group, indicating that the specimens fabricated by L-PBF have good structural and mechanical properties consistency.

In addition, Fig. 7(a-f) shows the comparison of compression results between FEA and experiment. It was found that these similar stress-strain curves all went through similar stages including linear growth, stress drop and stress plateau, showing the predictability of FEA with the Johnson-Cook damage model setting. The GSK and GSH curves show that the stress-strain response of the FEA model can accurately capture the yield strength and complex failure characteristics of the plateau stage for the structures. By simulating the performance prediction results with high reliability values, the mechanical strength of the additively manufactured gyroid structure is actually reproduced, indicating that the parameter setting of FEA is appropriate.

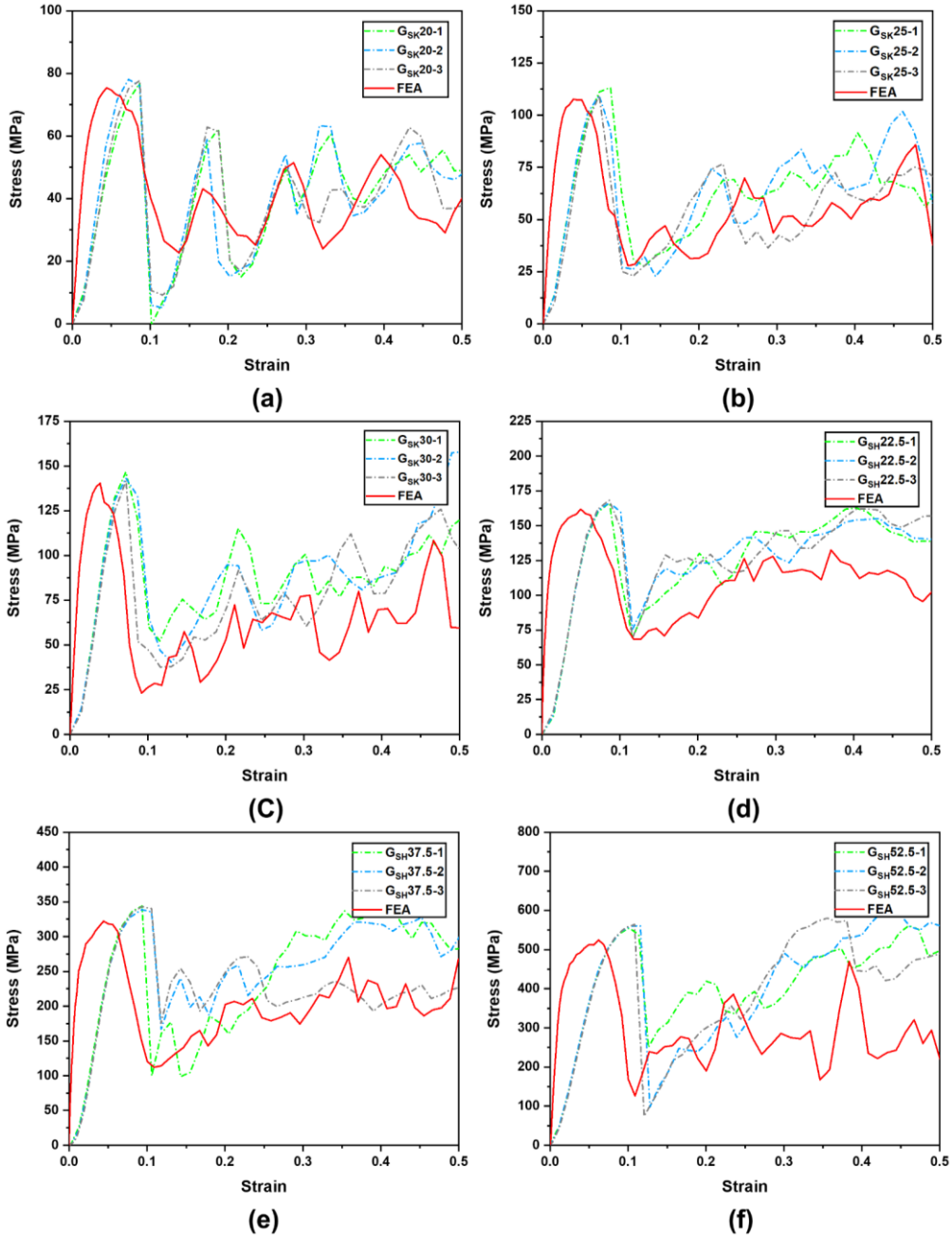

Fig. 7 Stress–strain curves of the gyroid structures: (a) $G_{SK}20$, (b) $G_{SK}25$, (c) $G_{SK}30$, (d) $G_{SH}22.5$, (e) $G_{SH}37.5$ and (f) $G_{SH}52.5$

Table 6 contains the values of elastoplastic properties obtained from the stress-strain curves in Fig. 7. The errors in the table are equal to ($Value_{FEA}$ - $Value_{EXP}$)/ $Value_{EXP}$. It is worth noting that the simulation values of the elastic modulus are larger than the experimental values. This situation, that the other properties are almost the same, but the elastic modulus value deviates greatly, is also reported in other studies. For example, there are also 72% and 74.9% errors in the work of Jin et al.[35] and Li

et al.[41], respectively. However, the main reason for the deviation of the Young's modulus in this study is the non-parallelism between the upper and lower surfaces of the specimen after wire cutting, which causes the loading area in contact with the compression plates to be smaller than the theoretical value before the peak stress is reached[42], resulting in a smaller real load collected under the same strain, i.e., the calculated Young's modulus is smaller.

The errors in yield strength and peak stress of simulation and experiment are essentially around 5%, which also proves that the simulation models provide reliable prediction of these two mechanical properties. There are two reasons why the experimental values of peak stress are larger than the simulation values. The first is that the specimen with a volume fraction slightly larger than the theoretical design value will have better mechanical properties. The second is that the size of the x and y axis of the specimen is slightly larger than the theoretical size (18 mm), see Fig. 5 (b). However, the theoretical area calculated by Equation (4) is slightly smaller than the actual area, so the peak stress of the experiment is larger than the simulation value.

Table 6 Elastoplastic properties of TPMS structures

Type	Elastic modulus (MPa)		Yield strength (MPa)		Peak stress (MPa)	
	EXP	FEA	EXP	FEA	EXP	FEA
$G_{SK}20$	1453.9±243	2266.4	61.9±1.3	65.4	77.9±0.2	75.4
	Δ=55.9%		Δ=5.7%		Δ=-3.2%	
$G_{SK}25$	2219.9±75.1	3497.3	88.9±3.5	103.3	110.7±2.2	107.7
	Δ=57.5%		Δ=16.2%		Δ=-2.7%	
$G_{SK}30$	3088.8±89.1	4805.7	115.2±6.4	122.3	143.9±2.5	140.4
	Δ=55.6%		Δ=6.2%		Δ=-2.4%	
$G_{SH}22.5$	3437.6±37.6	6689.1	126.5±1.7	131.9	167±1	160
	Δ=94.6%		Δ=4.3%		Δ=-4.2%	
$G_{SH}37.5$	6731.3±125.1	10932.2	266.2±2.7	272.6	342±2.8	322.1
	Δ=62.4%		Δ=2.4%		Δ=-5.8%	
$G_{SH}52.5$	8559.2±227.9	16658.7	423.6±12.2	426.5	558.3±5.3	524.7
	Δ=94.6%		Δ=0.7%		Δ=-6.0%	

The elastoplastic properties of G_{SK} and G_{SH} structures were further predicted and compared by using the Gibson–Ashby model, which is based on the results of the specimen experiments and simulation. In Gibson–Ashby model, $m_E = 1$ and $m_\sigma = 1$ are standard stretching-dominated porous structures, and $m_E = 2$ and $m_\sigma = 1.5$

are standard bending-dominated porous structures[43].

The constants E_0 and σ_0 calculated in this study, as discussed in Section 2.4, are 108090 MPa and 1189 MPa, respectively. These calculated parameters are listed in Table 7, while the relationship between the elastoplastic properties and the relative density of the gyroid structures is shown in Fig. 8. In contrast, the elastic modulus of G_{SH} shows the expected stretching-dominated ($m_E = 1$), which leads to much higher stiffness than G_{SK} bending-dominated ($m_E = 1.85$). Similarly, the strength of G_{SH} is closer to the stretching-dominated than G_{SK}, which is consistent with the conclusion of previous studies[24,25,33,44] by others that the sheet structures have better mechanical properties than skeletal structures. In addition, the strength of the simulation in Fig.8 (b) is basically consistent with the experimental value, and the fitted curves almost coincide, which also confirms the accuracy and reliability of the simulation.

Table 7 Constants of the Gibson–Ashby model of the gyroid structures

Type	Elastic modulus			Yield strength		
	C_E	m_E	R^2	C_σ	m_σ	R^2
G_{SK}-EXP	0.265	1.85	0.999	0.602	1.51	0.998
G_{SK}-FEA	0.404	1.83	0.999	0.599	1.44	0.954
G_{SH}-EXP	0.155	1.00	0.972	0.887	1.41	0.999
G_{SH}-FEA	0.313	1.12	0.994	0.868	1.37	0.999

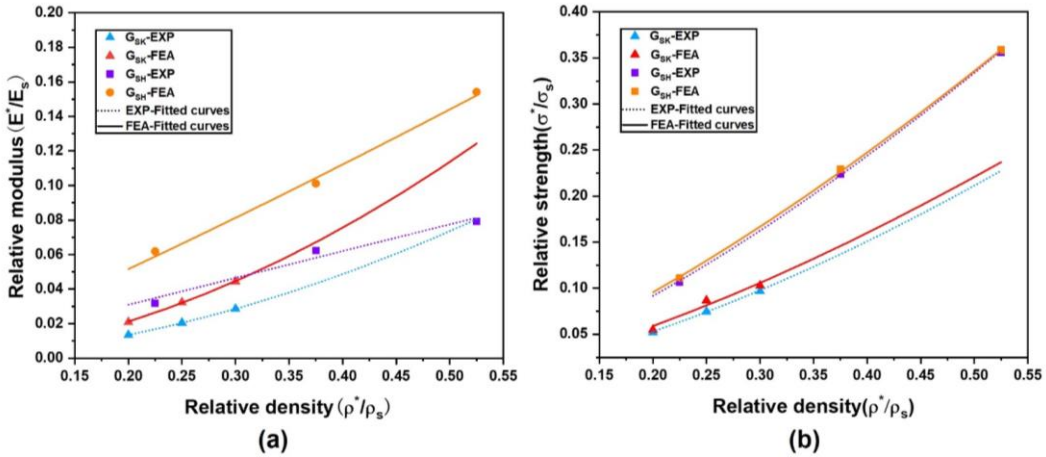

Fig. 8 Mechanical properties' prediction of gyroid structures using the Gibson–Ashby method: (a) relative modulus–density fitted lines of the gyroid structures and (b) relative strength–density fitted lines of the gyroid structures

3.3 Deformation Behaviour

The difference in mechanical properties between G_{SK} and G_{SH} structures is

reflected not only in the stress-strain curve but also in the failure-deformation behavior. Fig. 9 and Fig. 10 present the experimental and simulated mechanical response of G_{SK} and G_{SH} respectively. The results show that the failure mode of the simulation model is consistent with that of the experimental specimen. The results clearly show the plastic strain distribution characteristics of the lattice structure under quasi-static compression, which is of great significance for the study of the mechanism of deformation and failure.

For G_{SK} structures, Fig 9 shows that the stress is primarily concentrated at the center of the connection unit's support rod (ε=0.01). This finding is consistent with the phenomenon observed by Yánez et al.[45] and Yang et al.[32] using FE method. Because Gsk structures shows bending-dominated, the support rod is affected by bending, resulting in stress concentration. Therefore, it is recommended that the area with the highest stress in the center of these struts can be strengthened. When the strain reaches about 0.1, the bending-dominated structures begin to form local 45° and parallel fracture lines. As the strain increases ($0.1 \leqslant \varepsilon \leqslant 0.5$), the structure collapses layer by layer along the elements near the shear zone until densification, causing the stress-strain curves (see Fig. 7 (a-c)) to fluctuate significantly during the plateau stage.

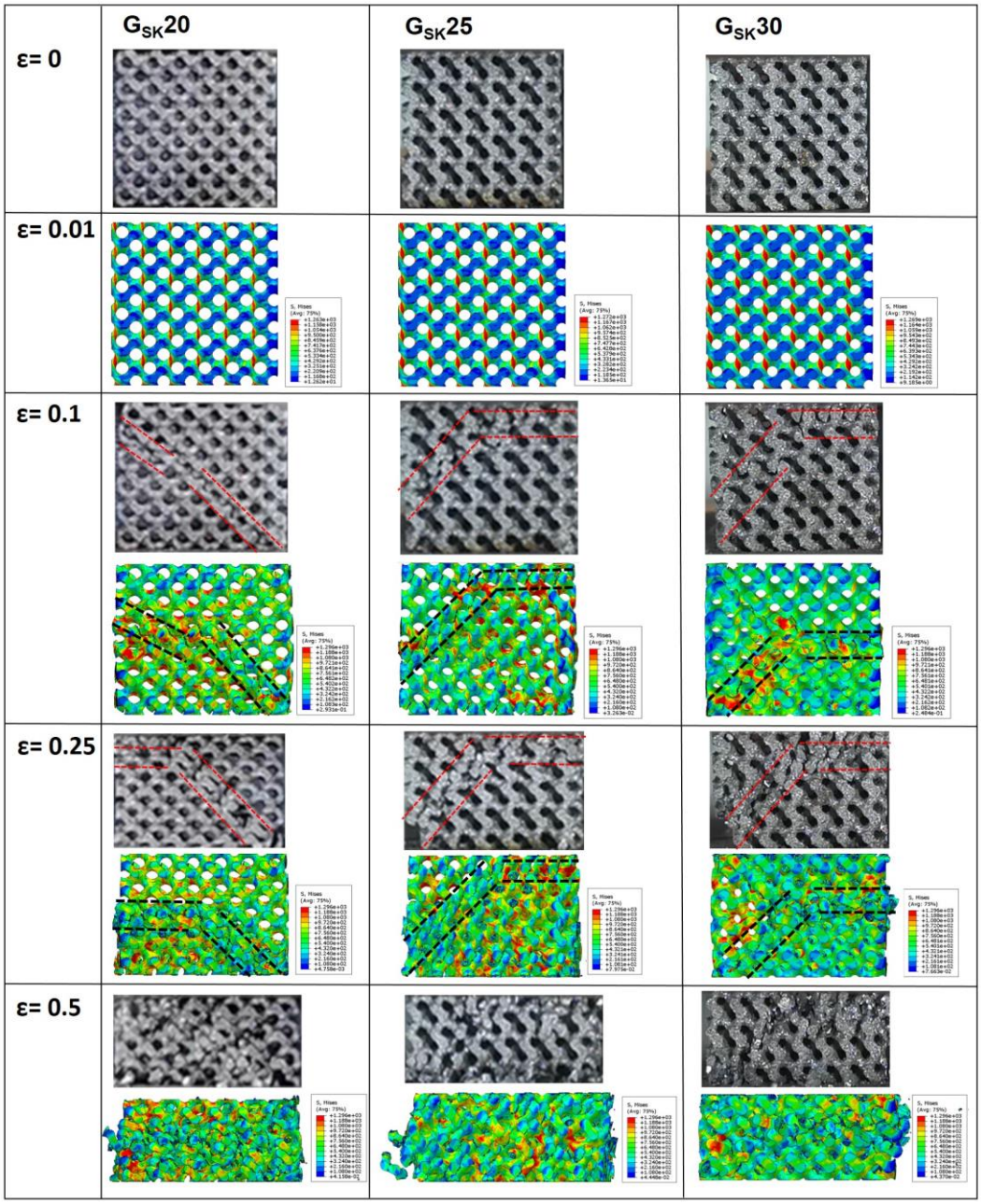

Fig. 9 Experimental and simulated failure deformation modes of G_{SK}

In the G_{SH} structure, stress is mainly concentrated on the part with maximum local curvature along the 45° direction (ε=0.01), resulting in a 45° shear failure along these parts (ε=0.1). With increasing strain ($0.1 \leqslant \varepsilon \leqslant 0.5$), the structure shows obvious horizontal sliding deformation along the direction of the fracture line, and the part with only a small number of units in contact with the top and bottom plates (the area shown in the circle) collapses layer by layer until densification. Compared with the collapsing deformation mode of G_{SK}, the more stable deformation behavior of G_{SH} makes the

stress-strain curve of the plateau stage more gentle.

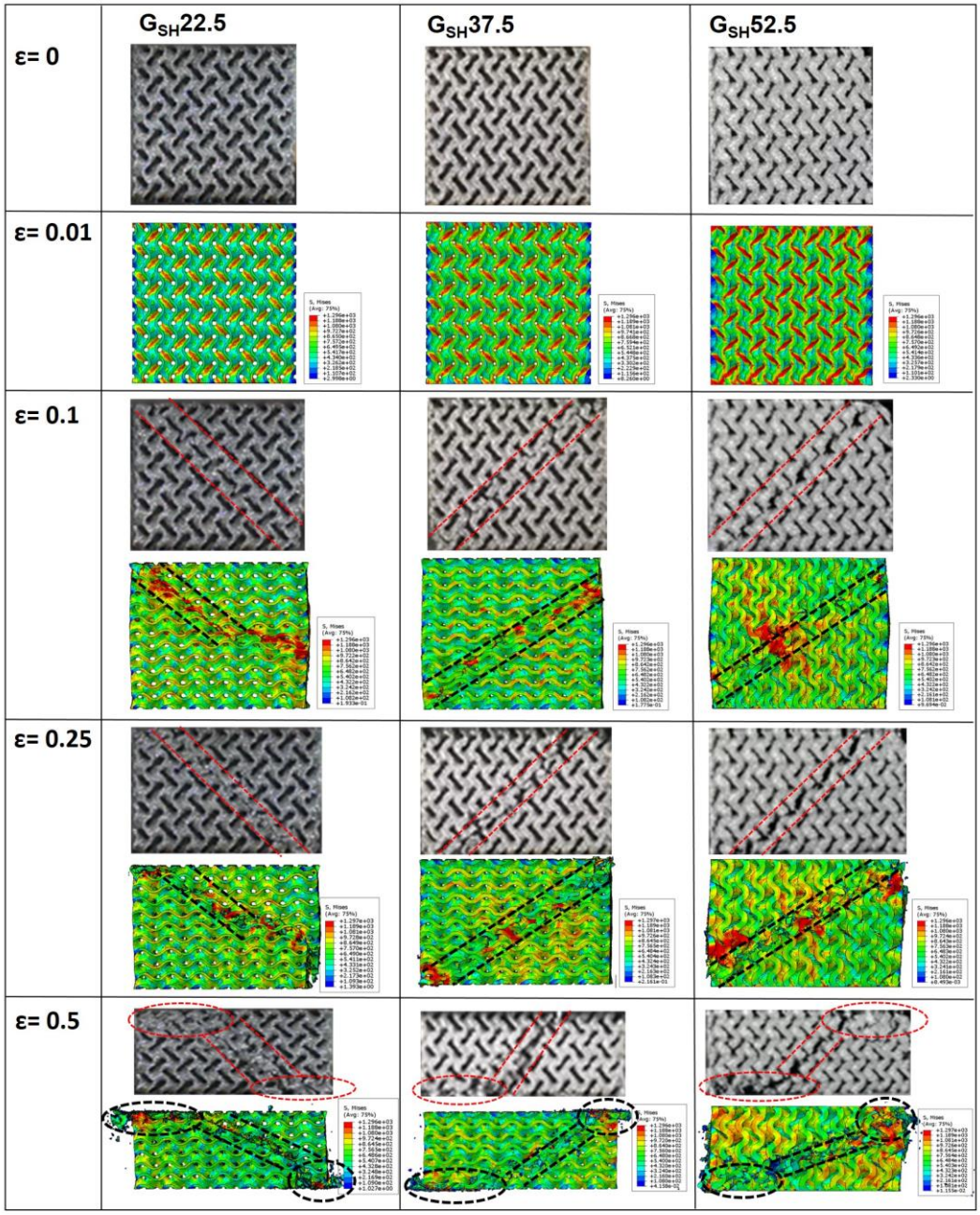

Fig. 10 Experimental and simulated failure deformation modes of G_{SH}

3.4 Energy Absorption Characteristics

Under compression load, TPMS structures have the ability to increase energy absorption at the same mass through the unique stress plateau phenomenon[26]. The strain range of energy absorption was chosen before densification ($0 \leqslant \varepsilon \leqslant 0.5$), so that the energy absorption in the plateau stress stage is better compared.

Energy absorption–strain (E-S) curves in Fig. 11(a) and (b) show the relationship

between the energy absorption of G_{SK} and G_{SH} and strain, and all curves are roughly divided into two stages: the elastic stage with a sharp increase in energy absorption ($0 \leqslant \varepsilon \leqslant 0.1$) and the plateau stress stage with a slow increase in energy absorption ($0.1 \leqslant \varepsilon \leqslant 0.5$). This is because the energy absorption mode of the structure in the elastic stage and the plateau stress stage is different. The elastic stage absorbs energy through elastic deformation, while the plateau stress stage absorbs energy through shear failure and layer-by-layer collapse.

In addition, the cumulative energy absorption-volume fraction (E-V) curves are shown in Fig.11(c) and (d), where the error of the small volume fraction of G_{SK} structures is only 0.1%-3.8%, while the error of the large volume fraction of G_{SK} (22.8%) and G_{SH} (10.6%-24.6%) is larger. The errors in the figures are equal to ($Value_{FEA}$ - $Value_{EXP}$)/ $Value_{EXP}$.This is due to the fact that the element after the structural fracture was automatically deleted when the Johnson-Cook damage model was set, resulting in the simulation results unable to show obvious densification phenomenon, which is more obvious in the large volume fraction structure (see Fig.7).

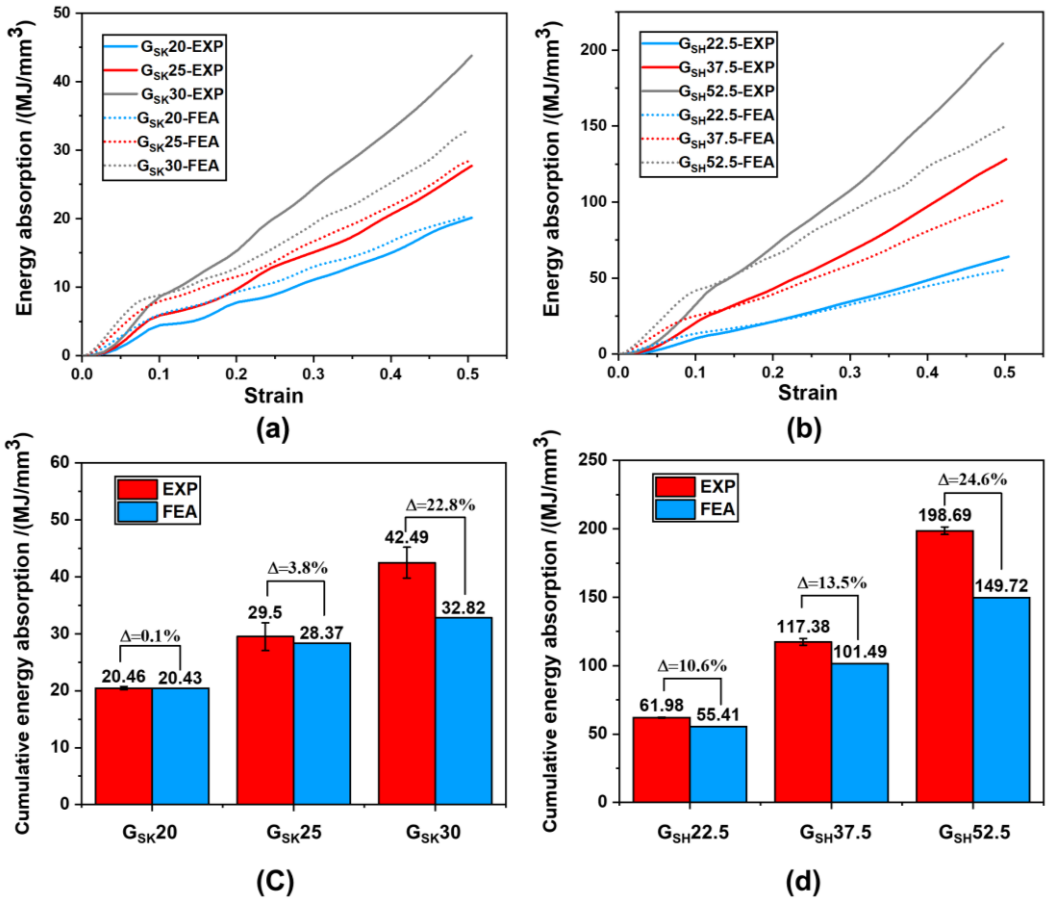

Fig. 11 (a) E-S curves of G_{SK} structures, (b) E-S curves of G_{SH} structures, (c) E-V curves of G_{SK} and (c) E-V curves of G_{SH} structures

Moreover, as shown in Fig 12, the energy absorption efficiency–strain (EAE-S) curves of the G_{SK} structure show a sharp fluctuation and a general upward trend, while the curves of the G_{SH} structure show a steady upward trend, which is consistent with the fluctuation of the corresponding stress-strain curves in Fig 7, which also proves that the G_{SH} structure has a more stable energy absorption capacity and can meet the requirements of high stability.

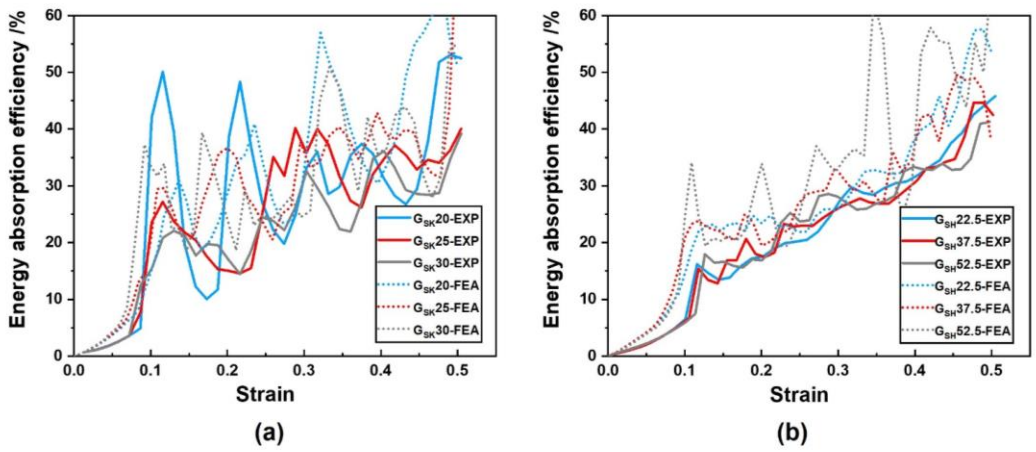

Fig. 12 EAE-S curves of gyroid structures: (a) G_{SK} structures and (b) G_{SH} structures.

4 Conclusions

In this study, two forms of gyroid structures, G_{SK} and G_{SH}, were designed and fabricated. In order to compare their manufacturability, mechanical properties and energy absorption properties, this study focused on the microtopography and defect distribution characteristics of three volume fractions of each structure. By combining high-precision simulation prediction based on the Johnson–Cook damage model and experimental verification, the study revealed the influence mechanism of the mechanical behavior, failure behavior and energy absorption characteristics of these two structures. The results of this study contributes to a more comprehensive understanding of the differences between G_{SK} and G_{SH} structures. The following conclusions can be drawn from this work:

1. The as-built specimens presented the expected shape and good manufacturability, with deviations in their volume fraction of 1.51%-2.56% (G_{SK}) and 8.38%-8.55% (G_{SH}), respectively. The larger specific surface area of the G_{SH} structure caused more unmelted powders and overhanging adhesions. This indicates that skeleton structures made of L-PBF have better manufacturability.
2. The mechanical properties were simulated and predicted with high reliability using the Johnson–Cook model. The error of yield strength and peak stress is about 5 %, which actually reproduced the mechanical strength of L-PBF-produced gyroid structures. Moreover, both experiments and simulations

indicate that the sheet structures have more stable energy absorption efficiency.

3. By comparing the prediction of Gibson–Ashby theory, it is proved that the G_{SH} structure is the stretching-dominated deformation, and its mechanical properties are better than those of G_{SK}structure by bending-dominated.
4. Compared with the layer-by-layer fracturing failure mode of the G_{SK} structure along the units near the fracture line, the G_{SH} structure experiences 45 ° diagonal shear and horizontal slip along the local part with maximum curvature, and only a small number of units in contact with the plates collapse layer by layer, which has a more stable stress platform stage and superior energy absorption capacity.

In conclusion, this study investigated the differences in manufacturability, mechanical behaviour and failure behavior, which is beneficial to guide the structural selection decision of various working conditions. Furthermore, the results show that the mechanical properties of specimens can be better predicted by FEA and Gibson–Ashby theory, and the cost and time of the experiment can be reduced to a certain extent, which is of great significance to reduce the resource consumption of gyroid structure performance research. In the future research, it is worth considering how to optimize the skeleton-gyroid and sheet-gyroid structures to improve their mechanical properties and energy absorption capacity, and how to combine the advantages of the two structures to design new structures that can adjust their mechanical properties according to the needs of lightweight.

CRediT authorship contribution statement

Zhichao Luo: Methodology, Software, Validation, Writing – original draft. **Qian Tang**: Supervision, Reviewing and editing. **Qixiang Feng**: Methodology, Supervision. **Shuai Ma**: Conceptualization. **Jun Song**: Formal analysis. Rossitza Setchi: Review & editing. **Fuyu Guo**: Investigation. **Yuanhang Zhang**: Software.

Declaration of competing interest

The authors declare that they have no known competing financial interests or personal relationships that could have appeared to influence the work reported in this paper.

Data Availability

Data will be made available on request.

Acknowledgment

This paper was supported by the National Natural Science Foundation of China (Grant No: 51975073, No. 51805052).

References

[1] F. Bobbert, K. Lietaert, A.A. Eftekhari, B. Pouran, S.M. Ahmadi, H. Weinans, A.A. Zadpoor, Additively manufactured metallic porous biomaterials based on minimal surfaces: a unique combination of topological, mechanical, and mass transport properties, Acta Biomater. 53 (2017) 572-584.

[2] M. Speirs, B. Van Hooreweder, J. Van Humbeeck, J. Kruth, Fatigue behaviour of niti shape memory alloy scaffolds produced by slm, a unit cell design comparison, J. Mech. Behav. Biomed. Mater. 70 (2017) 53-59.

[3] L. Han, S. Che, An overview of materials with triply periodic minimal surfaces and related geometry: from biological structures to self‐assembled systems, Adv. Mater. 30(17) (2018) 1705708.

[4] M. Kaur, K. Singh, Review on titanium and titanium based alloys as biomaterials for orthopaedic applications, Materials Science and Engineering: C 102 (2019) 844-862.

[5] S. Ma, Q. Tang, X. Han, Q. Feng, J. Song, R. Setchi, Y. Liu, Y. Liu, A. Goulas, D.S. Engstrøm, Manufacturability, mechanical properties, mass-transport properties and biocompatibility of triply periodic minimal surface (tpms) porous scaffolds fabricated by selective laser melting, Mater. Des. 195 (2020) 109034.

[6] R. Wauthle, J. Van Der Stok, S.A. Yavari, J. Van Humbeeck, J. Kruth, A.A. Zadpoor, H. Weinans, M. Mulier, J. Schrooten, Additively manufactured porous tantalum implants, Acta Biomater. 14 (2015) 217-225.

[7] Y. Wang, L. Huang, D. Mei, Y. Feng, M. Qian, Numerical modeling of microchannel reactor with porous surface microstructure based on fractal geometry, Int. J. Hydrog. Energy 43(49) (2018) 22447-22457.

[8] S. Catchpole-Smith, R. Sélo, A.W. Davis, I.A. Ashcroft, C.J. Tuck, A. Clare, Thermal conductivity of tpms lattice structures manufactured via laser powder bed fusion, Addit. Manuf. 30 (2019) 100846.

[9] H. Yin, F. Meng, L. Zhu, G. Wen, Optimization design of a novel hybrid hierarchical cellular structure for crashworthiness, Compos. Struct. 303 (2023) 116335.

[10] H. Yin, J. Zhou, G. Wen, Z. Wu, Crushing analysis and optimization for bio-inspired hierarchical 3d cellular structure, Compos. Struct. 286 (2022) 115333.

[11] Y. Chen, Z. Bai, L. Zhang, Y. Wang, G. Sun, L. Cao, Crashworthiness analysis of octagonal multi-cell tube with functionally graded thickness under multiple loading angles, Thin-Walled Struct. 110 (2017) 133-139.

[12] D. Barba, E. Alabort, R.C. Reed, Synthetic bone: design by additive

manufacturing, Acta Biomater. 97 (2019) 637-656.
[13] X. Zhang, G. Fang, S. Leeflang, A.A. Zadpoor, J. Zhou, Topological design, permeability and mechanical behavior of additively manufactured functionally graded porous metallic biomaterials, Acta Biomater. 84 (2019) 437-452.
[14] X. Zhang, X. Yan, G. Fang, M. Liu, Biomechanical influence of structural variation strategies on functionally graded scaffolds constructed with triply periodic minimal surface, Addit. Manuf. 32 (2020) 101015.
[15] G.S. Jung, M.J. Buehler, Multiscale mechanics of triply periodic minimal surfaces of three-dimensional graphene foams, Nano Lett. 18(8) (2018) 4845-4853.
[16] I. Maskery, N.T. Aboulkhair, A.O. Aremu, C.J. Tuck, I.A. Ashcroft, Compressive failure modes and energy absorption in additively manufactured double gyroid lattices, Addit. Manuf. 16 (2017) 24-29.
[17] A. Panesar, M. Abdi, D. Hickman, I. Ashcroft, Strategies for functionally graded lattice structures derived using topology optimisation for additive manufacturing, Addit. Manuf. 19 (2018) 81-94.
[18] F. Liu, Z. Mao, P. Zhang, D.Z. Zhang, J. Jiang, Z. Ma, Functionally graded porous scaffolds in multiple patterns: new design method, physical and mechanical properties, Mater. Des. 160 (2018) 849-860.
[19] W.E. Lee, 'cellular solids, structure and properties', Mater. Sci. Technol. 16(2) (2000) 233.
[20] C. Yan, L. Hao, A. Hussein, P. Young, D. Raymont, Advanced lightweight 316l stainless steel cellular lattice structures fabricated via selective laser melting, Mater. Des. 55 (2014) 533-541.
[21] J. Kadkhodapour, H. Montazerian, S. Raeisi, Investigating internal architecture effect in plastic deformation and failure for tpms-based scaffolds using simulation methods and experimental procedure, Materials Science and Engineering: C 43 (2014) 587-597.
[22] L. Wang, J. Lau, E.L. Thomas, M.C. Boyce, Co‐continuous composite materials for stiffness, strength, and energy dissipation, Adv. Mater. 23(13) (2011) 1524-1529.
[23] O. Al Ketan, R.K.A. Al Rub, R. Rowshan, Mechanical properties of a new type of architected interpenetrating phase composite materials, Adv. Mater. Technol. 2(2) (2017) 1600235.
[24][24] C.N. Kelly, J. Francovich, S. Julmi, D. Safranski, R.E. Guldberg, H.J. Maier, K. Gall, Fatigue behavior of as-built selective laser melted titanium scaffolds with sheet-based gyroid microarchitecture for bone tissue engineering, Acta Biomater. 94 (2019) 610-626.
[25][25] A.A. Zadpoor, Mechanical performance of additively manufactured meta-biomaterials, Acta Biomater. 85 (2019) 41-59.
[26][26] L. Zhang, S. Feih, S. Daynes, S. Chang, M.Y. Wang, J. Wei, W.F. Lu, Energy absorption characteristics of metallic triply periodic minimal surface sheet structures under compressive loading, Addit. Manuf. 23 (2018) 505-515.
[27] O. Al-Ketan, D. Lee, R.K.A. Al-Rub, Mechanical properties of additively-

manufactured sheet-based gyroidal stochastic cellular materials, Addit. Manuf. 48 (2021) 102418.
[28] X. Fan, Q. Tang, Q. Feng, S. Ma, J. Song, M. Jin, F. Guo, P. Jin, Design, mechanical properties and energy absorption capability of graded-thickness triply periodic minimal surface structures fabricated by selective laser melting, Int. J. Mech. Sci. 204 (2021) 106586.
[29] Q. Sun, J. Sun, K. Guo, L. Wang, Compressive mechanical properties and energy absorption characteristics of slm fabricated ti6al4v triply periodic minimal surface cellular structures, Mech. Mater. 166 (2022) 104241.
[30] H. Yin, Z. Liu, J. Dai, G. Wen, C. Zhang, Crushing behavior and optimization of sheet-based 3d periodic cellular structures, Composites Part B: Engineering 182 (2020) 107565.
[31] H. Wang, D. Tan, Z. Liu, H. Yin, G. Wen, On crashworthiness of novel porous structure based on composite tpms structures, Eng. Struct. 252 (2022) 113640.
[32][32] L. Yang, C. Yan, C. Han, P. Chen, S. Yang, Y. Shi, Mechanical response of a triply periodic minimal surface cellular structures manufactured by selective laser melting, Int. J. Mech. Sci. 148 (2018) 149-157.
[33][33] O. Al-Ketan, R. Rowshan, R.K.A. Al-Rub, Topology-mechanical property relationship of 3d printed strut, skeletal, and sheet based periodic metallic cellular materials, Addit. Manuf. 19 (2018) 167-183.
[34] A.M. Abou-Ali, D. Lee, R.K. Abu Al-Rub, On the effect of lattice topology on mechanical properties of sls additively manufactured sheet-, ligament-, and strut-based polymeric metamaterials, Polymers 14(21) (2022) 4583.
[35][35] M. Jin, Q. Feng, X. Fan, Z. Luo, Q. Tang, J. Song, S. Ma, Y. Nie, P. Jin, M. Zhao, Investigation on the mechanical properties of tpms porous structures fabricated by laser powder bed fusion, J. Manuf. Process. 76 (2022) 559-574.
[36] Z. Wang, P. Li, Characterisation and constitutive model of tensile properties of selective laser melted ti-6al-4v struts for microlattice structures, Materials Science and Engineering: A 725 (2018) 350-358.
[37] L.J. Gibson, M.F. Ashby, Cellular solids : structure and properties, Cellular solids : structure and properties, 1997.
[38] H.A. Almeida, P.J. Bártolo, Design of tissue engineering scaffolds based on hyperbolic surfaces: structural numerical evaluation, Med. Eng. Phys. 36(8) (2014) 1033-1040.
[39] I. Maskery, L. Sturm, A.O. Aremu, A. Panesar, C.B. Williams, C.J. Tuck, R.D. Wildman, I.A. Ashcroft, R.J. Hague, Insights into the mechanical properties of several triply periodic minimal surface lattice structures made by polymer additive manufacturing, Polymer 152 (2018) 62-71.
[40] D. Lee, K.A. Khan, R.K.A. Al-Rub, Stiffness and yield strength of architectured foams based on the schwarz primitive triply periodic minimal surface, Int. J. Plast. 95 (2017) 1-20.
[41] J. Li, Z. Zhao, R. Yan, Y. Yang, Mechanical properties of graded scaffolds developed by curve interference coupled with selective laser sintering, Materials Science and Engineering: C 116 (2020) 111181.

[42] M. Zhao, D.Z. Zhang, F. Liu, Z. Li, Z. Ma, Z. Ren, Mechanical and energy absorption characteristics of additively manufactured functionally graded sheet lattice structures with minimal surfaces, Int. J. Mech. Sci. 167 (2020) 105262.
[43] X.P. Tan, Y.J. Tan, C. Chow, S.B. Tor, W.Y. Yeong, Metallic powder-bed based 3d printing of cellular scaffolds for orthopaedic implants: a state-of-the-art review on manufacturing, topological design, mechanical properties and biocompatibility, Materials Science and Engineering: C 76 (2017) 1328-1343.
[44] S.C. Kapfer, S.T. Hyde, K. Mecke, C.H. Arns, G.E. Schröder-Turk, Minimal surface scaffold designs for tissue engineering, Biomaterials 32(29) (2011) 6875-6882.
[45] A. Yánez, A. Cuadrado, O. Martel, H. Afonso, D. Monopoli, Gyroid porous titanium structures: a versatile solution to be used as scaffolds in bone defect reconstruction, Mater. Des. 140 (2018) 21-29.